Available online at www.sciencedirect.com
ScienceDirect
Trans. Nonferrous Met. Soc. China 34(2024) 846−860
Transactions of Nonferrous Metals Society of China
www.tnmsc.cn

Optimization of additive manufactured Ti-based pyramidal lattice structure applied to interface strengthening of Mg/Ti bimetal composites

Yuan-bing WU[1], Jian-hua ZHAO[1,2], Wei-li PENG[1], Cheng GU[1,2], Jin CHENG[1], Ya-jun WANG[1,2]

1. College of Materials Science and Engineering, Chongqing University, Chongqing 400045, China;
2. National Engineering Research Center for Magnesium Alloys, Chongqing University, Chongqing 400044, China

Received 17 August 2022; accepted 31 December 2022

Abstract: Mg/Ti bimetal composites were fabricated by ultrasonic-assisted solid−liquid compound casting with an additively manufactured Ti-based pyramidal lattice structure at the interface. The Taguchi method was carried out to optimize the lattice parameters. The optimized geometric parameters include: the strut diameter (d) is 1 mm, the ratio of strut length to diameter (l/d) is 3, and the ratios of the upper and lower node to diameter (d_1/d and d_2/d) are 2.5 and 2.5, respectively. The ratio of strut length to diameter is the most significant factor affecting failure strength. The failure strength of the Mg/Ti bimetal joint with the optimized lattice structure is 77.3 MPa. Experimental and simulated results show that the failure strength increases first and then decreases with the increase of l/d, and it reaches the peak value when l/d is 3.

Key words: Mg/Ti bimetal composites; pyramidal lattice structure; optimization; additive manufacturing; failure strength; finite element analysis

1 Introduction

The requirement for lightweight structural materials is becoming increasingly urgent for energy conservation and emission reduction [1]. Utilizing the complementary properties of Ti (high temperature, excellent corrosion resistance, and a high specific strength) and Mg (high specific strength and specific stiffness), Mg/Ti bimetal composites have great potential for applications where mass reduction is important as well as mechanical property [2−4]. Thus, different joining techniques have been developed to fabricate Mg/Ti bimetal composites, i.e., high-pressure sintering [5], powder metallurgy [6], laser welding-brazing [7], transient liquid phase bonding [8], friction stir welding [9], hot roll bonding [10], and so on.

Compared with other methods, solid−liquid compound casting (SLCC) has the advantages of low production cost and a simple processing procedure [11−13]. The most obvious characteristic of SLCC is that it can produce bimetallic castings with complex shapes and internal structures [4]. The interfacial bonding strength determines the properties of composites, and interface strengthening has always been a hotspot in the field of SLCC [12−14]. However, the large incompatibility between Ti and Mg, such as immiscibility (maximum solid solubility of Ti in Mg is 0.02 at.% and that of Mg in Ti is 0.9 at.%) and large discrepancy in the melting point (1678 °C for Ti and 650 °C for Mg), brings great challenges to their robust bonding [5]. Existing studies have fabricated Mg/Ti bimetals with a metallurgical bonding interface by adding intermediate layer metals such as Ni [7,8,15], Cu [16−18], Zn [19], and Al [20,21]. However, the addition of interlayer

Corresponding author: Cheng GU, Tel: +86-15077857283, E-mail: gucheng.90@cqu.edu.cn
DOI: 10.1016/S1003-6326(23)66438-6

leads to the formation of a thick intermetallic layer, which not only obstructs atomic diffusion and decreases the bonding strength of joints [4] but also deteriorates the physical properties such as heat resistance, electrical conductivity, and heat conduction [16]. Therefore, finding a new method to fabricate Mg/Ti bimetal casting is necessary.

Due to their fully-open interior space, three-dimensional lattice structures with light-weight, excellent specific strength and specific stiffness, and high specific surface area have received extensive attention [22,23]. Moreover, the advent of additive manufacturing (AM) technology makes the fabrication of lattice structures with complex geometries possible [24]. Various lattice structural and open-cell topological configurations have been designed [25], in which the pyramidal lattice structures have a variety of excellent mechanical characteristics including higher strength and buckling resistance, lower relative density, and higher specific strength [26]. Recently, the lattice materials were applied to improving the interface bonding of composite. This kind of latticed composite contains two parts, namely the lattice and the matrix, in which lattice structures have been infilled in the matrix to improve the interface bonding of composite, such as steel/Al [27], Al/NiTi [28], carbon fiber/steel [29], and A356/316L interpenetrating phase composites [30]. However, lattice materials have not been applied to the interface connection of Mg/Ti dissimilar metals, and the strengthening mechanism is still unknown.

In this work, Ti-based pyramidal lattice structures were fabricated by selective laser melting (SLM), and the lattice structure was applied in the interface bonding of Mg/Ti bimetal composite. The direct combination of magnesium and titanium alloys was realized by making full use of the high specific area of lattice structures to form a three-dimensional embedded structure with the magnesium matrix. The Mg/Ti bimetal composites formed by TC4 lattice and AZ91D melt were fabricated by ultrasonic-assisted SLCC. Finite element (FE) and experimental methods were used to optimize the lattice structure and investigate the lattice structure's strengthening mechanism to the interface of Mg/Ti bimetal composites.

2 Finite element simulation

2.1 Geometric model

This study is to make full use of the high specific area of TC4 lattice structure and to form three-dimensional inter-embedded structures with magnesium alloys. The pyramidal lattice structure was chosen since it has the advantages of simple configuration, low density, high strength, and anti-buckling performance [26]. Taking the dimensional accuracy and manufacturability of the lattice structure fabricated by SLM into account, the diameter of the lattice structure (d) can be adjusted in the range of 0.4−1.8 mm [31]. The designed monolayer lattice structure, as shown in Fig. 1(a), consists of four inclined cylindrical struts with an incline angle ω of 45° and α of 45°. To ensure the stability and reliability of the lattice structure, the spherical joints are used to connect each strut element. In Fig. 1(a), the geometrical parameters of the unit cell include the length (a), the width (b), the strut diameter (d), the strut length (l), and the upper and lower rod diameter (d_1, d_2). Figure 1(b) shows the structure of the Mg/Ti bimetal composite, which is comprised of two parts. The upper semi-transparency part is the magnesium matrix. The lower part, constituted by periodically arranged unit cells, is the designed TC4 lattice structure.

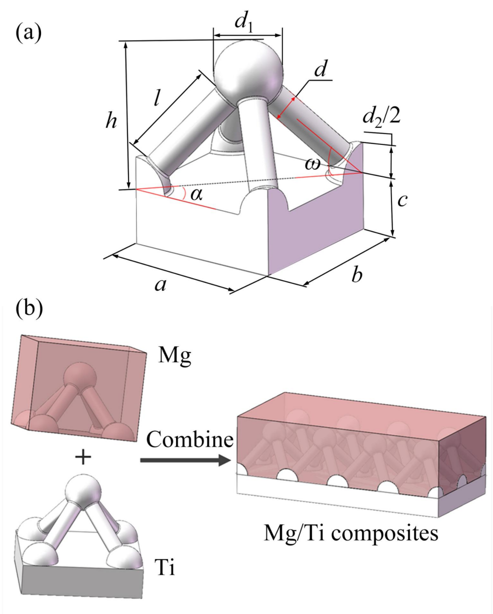

Fig. 1 Illustrations of Mg/Ti bimetal composite: (a) Unit cell of TC4 lattice structure; (b) Geometry of Mg/Ti bimetal composite with designed TC4 lattice structure

2.2 Model simplification and mesh generation

The numerical model of the Mg/Ti bimetal composites was built by the finite element method, and the quasi-static tensile process was simulated by using the dynamic/explicit solver of ABAQUS software [32]. Researchers, due to the low computational cost and acceptable results in quasi-loading conditions, often used the unit cell method instead of the entire lattice structure [33] and a quarter of a unit cell lattice model was used as the calculation object to establish the FE model. This structure has been meshed using modified tetrahedral elements with quadratic interpolation. The diagram of mesh division is shown in Fig. 2(a). The element size was estimated by performing a mesh sensitivity analysis, leading to different models that are composed of different numbers of elements from 153135 to 537078. To reduce the influence of stress concentration on the analysis results caused by sudden changes in local size, as shown in Fig. 2(b), the joints between the struts and nodes are transitioned by an arc. According to the principle of master-slave surface setting [32], the surface of the lattice structure with greater rigidity is defined as the master surface, and the inner surface of the magnesium matrix in contact with the lattice structure is the slave surface.

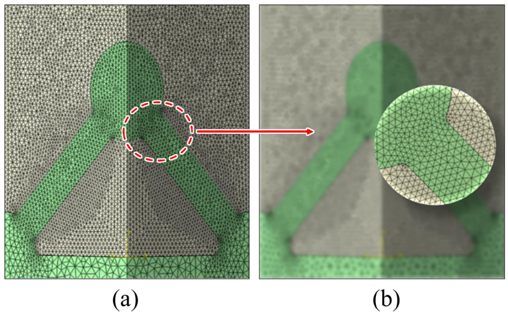

Fig. 2 A quarter of finite element model of Mg/Ti composite: (a) Schematic diagram of mesh division of whole structure; (b) Detail of local mesh

2.3 Materials and property parameters

To simulate the mechanical characterization of Mg-AZ91D/Ti−TC4 bimetal composite, the constitutive model of AZ91D and TC4 are already implemented within the software material library and their parameters are identified on tensile stress−strain curves obtained from full dense stand specimens. Figure 3(a) shows the geometric dimensions of samples used for the tensile test. The tensile rate was set to be 0.5 mm/min. Each type was tested three times, and the arithmetic mean value was taken as the representative value. The stress−strain curves of as-cast AZ91D and AM Ti−6Al−4V alloy are shown in Fig. 3(b). The property parameters of Ti−6Al−4V and AZ91D are shown in Table 1. Besides, several assumptions are considered during the FE analysis. Firstly, the lattice material is assumed to be isotropic material, and the tensile stress−strain relationships are the same for each other. Secondly, the cross-section of all struts is assumed to be circular, with a constant diameter d. Thirdly, the Mg/Ti composite ingot is also assumed to be an ideal material with an upper bound of mechanical properties.

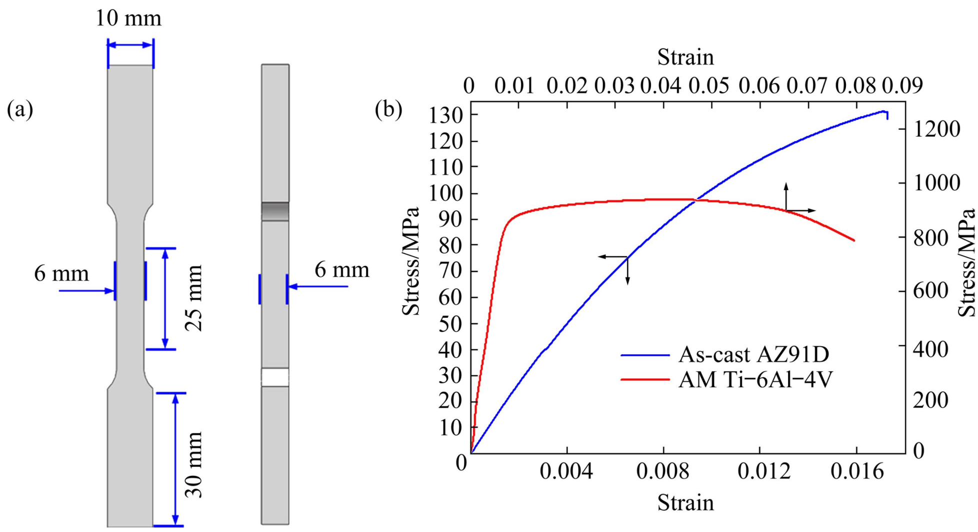

Fig. 3 Tensile specimens and tensile stress−strain curves: (a) Geometric dimensions of tensile specimens; (b) Tensile stress−strain curves of as-cast AZ91D and additive manufactured Ti−6Al−4V

Table 1 Property parameters of materials

Material	Density/ $(g\cdot cm^{-3})$	Young's modulus/ GPa	Poisson ratio	Yield strength, σ_s/MPa	Ultimate tensile strength, σ_b/MPa
AZ91D	1.82	44.8	0.35	92.7	131.4
Ti−6Al−4V	4.43	118	0.34	944	1058

2.4 Boundary conditions and interface behavior

In the numerical tensile tests, the boundary conditions, as shown in Fig. 4, were as follows: (1) the bottom face was completely fixed and the upper face was pulled by a constant force, and (2) classical symmetrical boundary conditions were applied to the four lateral sides.

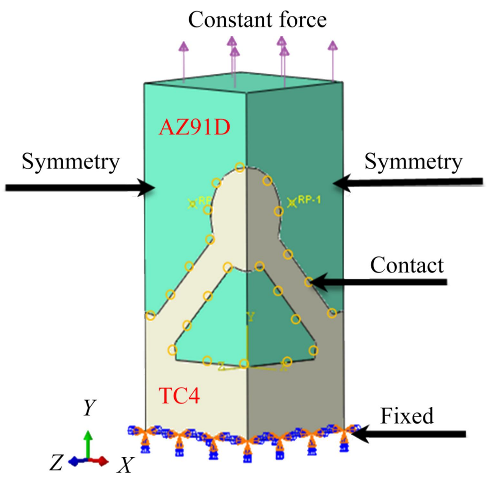

Fig. 4 FE model of Mg/Ti bimetals and boundary conditions

The general contact with hard contact, frictionless properties, and cohesive behavior was considered. The interface behavior between AZ91D and TC4 was simplified to the traction-separation law. The available traction-separation model in Abaqus assumes initially linear elastic behavior followed by the initiation and evolution of damage [32]. The elastic behavior is written in terms of an elastic constitutive matrix that relates the normal and shear stresses to the normal and shear separations across the interface. Damage initiation refers to the beginning of degradation of the cohesive response at a contact point. The onset of damage was dictated by a maximum stress criterion, which is expressed mathematically as

$$\max\left\{\frac{\langle t_n\rangle}{t_n^0},\frac{t_s}{t_s^0},\frac{t_t}{t_t^0}\right\}=1 \tag{1}$$

where $\langle t_n\rangle$ represent the Macaulay brackets, which returns the argument if positive and zero otherwise to impede the development of damage when the interface is under compression; t_n^0, t_s^0, t_t^0 represent the peak values (t_n, t_s, t_t represent the actual values) of the contact stress when the separation is either purely normal to the interface or purely in the first or the second shear direction, respectively. For simplicity, t_n^0, t_s^0, t_t^0 were assumed to be equal ($t_n^0=t_s^0=t_t^0=\sigma_{max}$) to the interface strength σ_{max} (25 MPa), which was obtained by the shear test of the TC4/AZ91D bimetals [15]. To simulate the tensile test, as shown in Fig. 4, uniform surface pressure was loaded on the upper surface by defining a loading Time-Amplitude curve with an inclination angle of 45°. And then, the failure time was read and the failure load was calculated according to the loading curve, and the failure load pressure was defined as the failure strength of the Mg/Ti bimetal composite. The results of the FE simulations were analyzed by the S/N and ANOVA. Finally, optimal geometrical parameters of lattice structures can be obtained.

3 Experimental

3.1 Manufacturing of lattice structure

For the fabrication of the lattice structures, ASTM Ti−6Al−4V spherical powder with a particle size of 15−53 μm was used. The chemical composition of the TC4 powder is listed in Table 2.

Table 2 Chemical composition of TC4 powder (wt.%)

Al	V	O	Fe	C
6.38	3.93	0.17	0.27	0.013
H	N	Cu	Sn	Ti
0.003	0.0072	0.091	0.01	Bal

A commercial selective laser melting (SLM) machine (BLT-S210, Xi'an, China) was used to fabricate the lattice structures. The key technological parameters used during the SLM are listed in Table 3.

Table 3 SLM process parameters used for manufacturing lattice structure

Laser power/W	Spot diameter/μm	Scanning speed/ (mm·s^{-1})	Hatch spacing/μm	Layer thickness/μm	Atmosphere
155	60	1200	90	30	Ar

To further improve the dimensional stability and mechanical properties of the specimen fabricated by SLM, the heat treatment process of stress-relieving annealing was performed in a vacuum at 800 °C for 2 h and hereafter cooled to 300 °C with the furnace slowly at a flowing argon atmosphere, and then air-cooled to ambient temperature [34].

3.2 Solid−liquid compound casting process

Before casting, the TC4 lattice specimens were degreased in an alkali cleaner composed of NaOH 70 g/L, Na_2CO_3 30 g/L, Na_3PO_4 20 g/L, Na_2PO_3 7 g/L at 80 °C for 10 min. And then, the acid solution containing 30% hydrofluoric, and 70% nitric acid was used to remove the oxide film on the surface of the TC4 specimen at room temperature for 2 min. After that, the pickled TC4 lattice specimen was pretreated at 350 °C in a heat treatment furnace with a vacuum degree of 1.33×10^{-3} Pa and kept at the temperature for 30 min. The commercial magnesium alloy AZ91D (Mg−9%Al−1%Zn) was used as a molten magnesium bath to fabricate the TC4/AZ91D bimetallic castings. The AZ91D ingots were melted under the protection of a mixture of CO_2 and 0.5% SF6 in a stainless-steel crucible, which was located in an electrical resistance furnace at an elevated temperature from ambient temperature to 730 °C.

Figure 5 shows the schematic illustration of the solid−liquid compound casting process. The ultrasonic horn was immersed into the melt to improve the fluidity of AZ91D magnesium alloy melt by the ultrasonic resonant transducer with a frequency of 30 kHz and an input power of 12 kW [35]. The customized mold was also preheated in a box-type furnace at 350 °C for 2 h. And then, the AZ91D melts were poured into the mold with a steady casting speed.

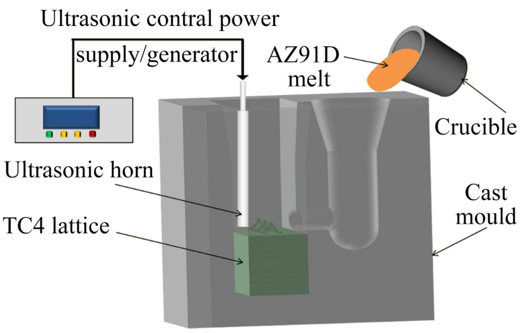

Fig. 5 Schematic illustration of solid−liquid compound casting

3.3 Tensile test

Tensile tests were performed to study the failure strength of the Mg/Ti bimetal joints. Figure 6(a) shows the tensile test sampling position from the Mg/Ti bimetallic ingot, which is the region of the TC4 lattice structure and AZ91D interlocked. Figure 6(b) illustrates the specific dimensions of the tensile specimen of each lattice structure. Three tensile specimens were prepared for each lattice structure to minimize the experimental error.

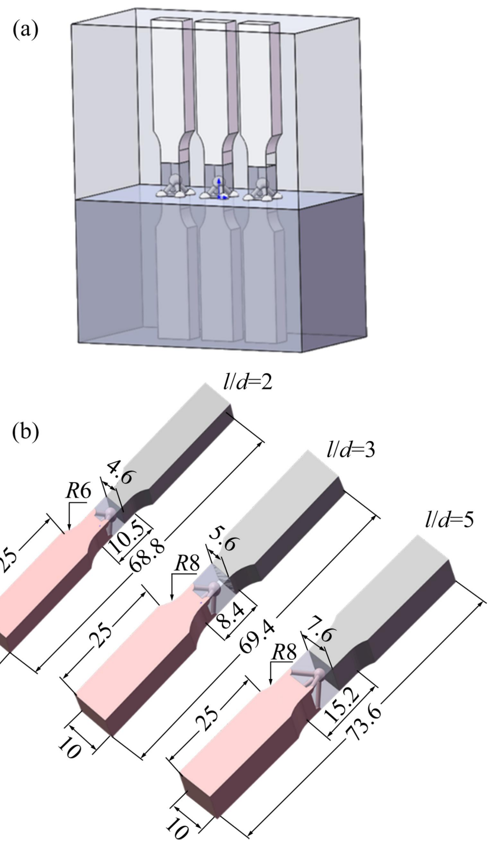

Fig. 6 Sampling position and size of composite tensile specimen: (a) Sampling position of Mg/Ti tensile specimen; (b) Tensile specimen size for *l*/*d* of 2, 3, and 5

4 Results and discussion

4.1 Optimization of lattice structure

As illuminated in Figure 1(a), among the interrelated geometrical parameters, the strut diameter (d), the strut length (l), and the upper and lower rod diameter (d_1, d_2) are paramount to the mechanical properties. Therefore, it is necessary to investigate a better combination of those parameters within the strut diameter range of 0.4−1.8 mm. The Taguchi orthogonal array (OA) gives unique combinations between parameters and their levels to minimize the number of experiments while still investigating the entire parameter space [36], so it was used to optimize the geometrical parameters of the lattice structure. Three levels of these parameters were designed and listed in Table 4.

Table 4 Designed parameters and levels

Symbol	Parameter	Level 1	Level 2	Level 3
A	Strut diameter, d/mm	0.6	1	1.4
B	Ratio of strut length to diameter, l/d	2	3	4
C	Ratio of upper node diameter to strut diameter, d_1/d	2.5	2.8	3.1
D	Ratio of lower node diameter to strut diameter, d_2/d	2.5	2.8	3.1

Since the interaction between the geometrical parameters was not considered, there are eight degrees of freedom owing to the four geometrical parameters with three levels. The Orthogonal analysis was performed based on the FE simulations. The failure strength of the composite was defined as the maximum load that the material can sustain under uniaxial tensile loading. Table 5 provides the details and FE analysis results of the L9 scheme (3^4), a standard orthogonal plan proposed by Taguchi [37].

The S/N (signal-to-noise) ratio is used by the Taguchi method, which measures the quality characteristic deviating from the desired value [36]. The S/N ratio was calculated from the following equations:

$$\mathrm{S/N}=-10\lg\left(\frac{1}{n}\sum_{i=1}^{n}\frac{1}{X_i^2}\right) \tag{2}$$

where n is the number of tests, and X_i is the value of failure strength for the ith experiment.

Table 6 shows the S/N ratio of FE analysis results for failure strength. The mean S/N ratio for each level of the parameters is calculated and then the maximum minus minimum value is calculated.

Table 5 Orthogonal plans and FE analysis results for failure strength

Experimental No.	Parameter level				Failure strength/MPa
	A/mm	B	C	D	
1	0.6	2	2.5	2.5	46.6
2	0.6	3	2.8	2.8	47.5
3	0.6	4	3.1	3.1	39.2
4	1	2	2.8	3.1	46.9
5	1	3	3.1	2.5	51
6	1	4	2.5	2.8	40.8
7	1.4	2	3.1	2.8	40.1
8	1.4	3	2.5	3.1	49
9	1.4	4	2.8	2.5	38

Table 6 S/N response for failure strength

Symbol	Parameter	Mean S/N ratio			Range	Rank
		Level 1	Level 2	Level 3		
A	d	32.922	33.265	32.489	0.776	2
B	l/d	32.953	33.832	31.892	1.940	1
C	d_1/d	33.128	32.851	32.697	0.431	4
D	d_2/d	33.040	32.605	33.031	0.435	3

The total mean S/N ratio=32.892 dB.

The strut length to diameter is ranked as 1, indicating that its effect is the most significant for increasing (and vice versa) failure strength than other parameters. Figure 7 shows the S/N response graph for failure strength. As shown in Eq. (2), the greater the S/N ratio, the smaller the variance of failure strength around the desired (the higher-the-better) value. However, the relative importance of the geometrical parameters still needs to be known so that optimal combinations of the parameter levels can be determined more accurately.

Nominal control of the final response requires knowledge of the significant effect of individual parameters on the quality characteristic, which can

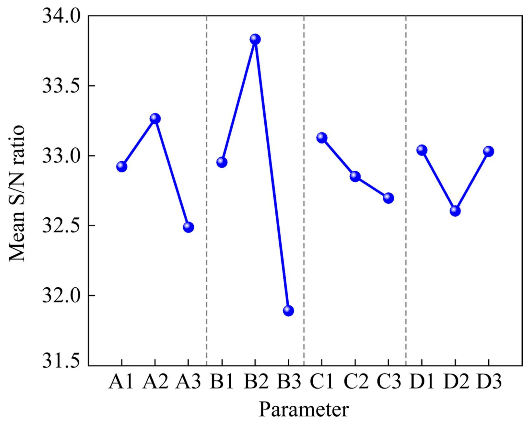

Fig. 7 S/N graph for failure strength of composite

be estimated using a statistical method, namely analysis of variance (ANOVA) [38]. Table 7 shows the results of the ANOVA. It can be found that the *l*/*d* is the most significant parameter for affecting the failure strength of Mg/Ti composites. Based on the S/N and AVOVA analysis, the optimal geometrical parameters of the lattice structure are the strut diameter at level 2 (d=1 mm), the ratio of strut length to the diameter at level 2 (l/d=3), and the ratio of the up and lower node to the diameter at level 1 (d_1/d=2.5) and level 2 (d_1/d=2.5), respectively.

The predicted S/N ratio η for the optimal level can be calculated by [39]

$$\eta=\eta_{\mathrm{m}}+\sum_{i=1}^{n}(\overline{\eta}_i-\eta_{\mathrm{m}}) \tag{3}$$

where η_{m} is the total mean S/N ratio, $\overline{\eta}_i$ is the mean S/N ratio at the optimal level, and n is the total number of the main design parameters that affect the quality characteristic.

The estimated S/N ratio using the optimal parameters can then be obtained and the corresponding failure strength can also be calculated by using Eq. (3). Table 8 shows the results of the calculation and FE analysis, and the error is 4.4% between the two values. The failure strength of Mg/Ti composites is 56 MPa obtained by FE analysis at the optimized lattice structure parameters.

4.2 Effect of ratio of strut length to diameter (*l*/*d*)

Based on the optimal combination of geometrical parameters, six groups of single-factor experiments were conducted to investigate the sensitivity of significant parameters (l/d). The other parameters are constants with orthogonal optimal analysis (d=1, d_1/d=2.5, d_2/d=2.5). Figure 8 shows the results of numerical experiments of tensile tests with varied strut lengths to diameters. The failure strength of the Mg/Ti bimetallic joints shows a parabolic trend with the increase of strut length to diameter (l/d) of the TC4 lattice structure. The failure strength increases nonlinearly with the l/d and reaches a peak value when the l/d is equal to 3, and then decreases with further increase of l/d.

Here, the rule-of-mixtures by simply treating the composite as the sum of Mg and TC4 lattice structure were presented for comparison, as indicated by the dash curves in Fig. 8. Specifically, the ultimate strength of the composite, σ_{ROM}, was approximated by summing that of AZ91D, σ_{Mg}, and TC4 lattice structure, σ_{Ti}, weighted by its volume fraction, V_{Mg}, and V_{Ti}, following the relation $\sigma_{\mathrm{ROM}}=\sigma_{\mathrm{Mg}}V_{\mathrm{Mg}}+\sigma_{\mathrm{Ti}}V_{\mathrm{Ti}}$, where the volume fraction of TC4 lattice structure (V_{Ti}) in the composite can be calculated.

In a unit cell, as shown in Fig. 1(a), the relative volume fraction of lattice structure, V_{OL}, can be defined as the volume ratio of the lattice to the solid body of the same thickness, V_{Solid}, which can be calculated by the formula of $V_{\mathrm{OL}}=V_{\mathrm{Lattice}}/V_{\mathrm{solid}}$. V_{Lattice} is equal to the sum of the volume of the upper node (VUN), the four struts (VS), and half of

Table 7 Results of analysis of variance

Symbol	Parameter	Degree of freedom	Sum of square	Mean square	*F*	Contribution/%
A	*d*	2	0.907	0.454	3.153	12.069
B	l/*d*	2	5.663	2.832	19.667	75.356
C	d_1/d	2	0.287	0.144	1	3.819
D	d_2/d	2	0.371	0.186	1.292	4.937
Error		2	0.287	0.144		3.819
Total		10	7.515			100

Table 8 Results of calculation and FE analysis at optimized lattice structure parameters

A2B2C1D1	Failure strength/MPa	S/N ratio/dB	Error/%
Prediction	53.64	34.59	4.4
FE analysis	56	34.96	4.4

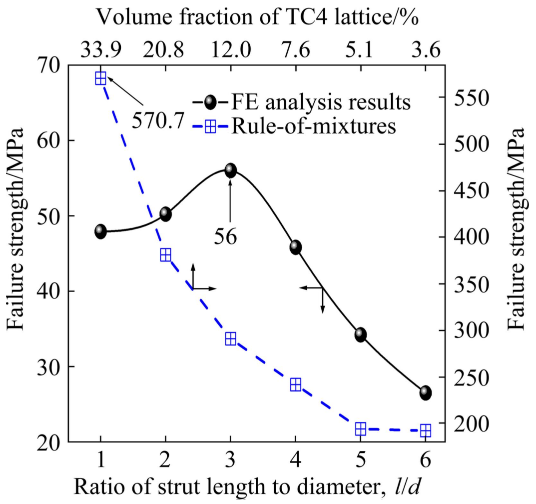

Fig. 8 Failure strength with ratio of strut length to diameter and its comparison with that obtained by rule-of-mixture

the volume of the lower node (V_{LN}), depending on its architecture. The volume of the lattice, $V_{Lattice}$, can be expressed approximately as

$$V_{Lattice}=V_{UN}+4V_S+V_{LN}/2 \tag{4}$$

where $V_{UN}=\pi d^3O_1^3/6$, $V_S\approx\pi d^3H/4$, $V_{LN}=\pi d^3O_2^3/6$, $O_1=d_1/d$, $O_2=d_2/d$, and $H=l/d$.

The volume of solid body V_{solid} can be written as

$$V_{Solid}=abh \tag{5}$$

where $a=b\approx d(O_1+O_2+2H)\cos\omega\cdot\cos\alpha$, $h\approx d\sin\omega\cdot(O_2+2H)/2+dO_1(1+\sin\omega)/2$, and $\omega=\alpha=45°$.

It can be seen that V_{Ti} decreases with the increase of l/d, but the failure strength of the composite is not consistent with the change of volume fraction of the reinforced body. This is different from the report in that the mechanical properties of composites are positively correlated with the volume fraction of the reinforcement phase [2,3,6]. This can be ascribed to the characteristics of the lattice structure and its interaction with the magnesium matrix.

Figure 9 shows the contour plots of the von-Mises equivalent stress (MISES). As can be seen,

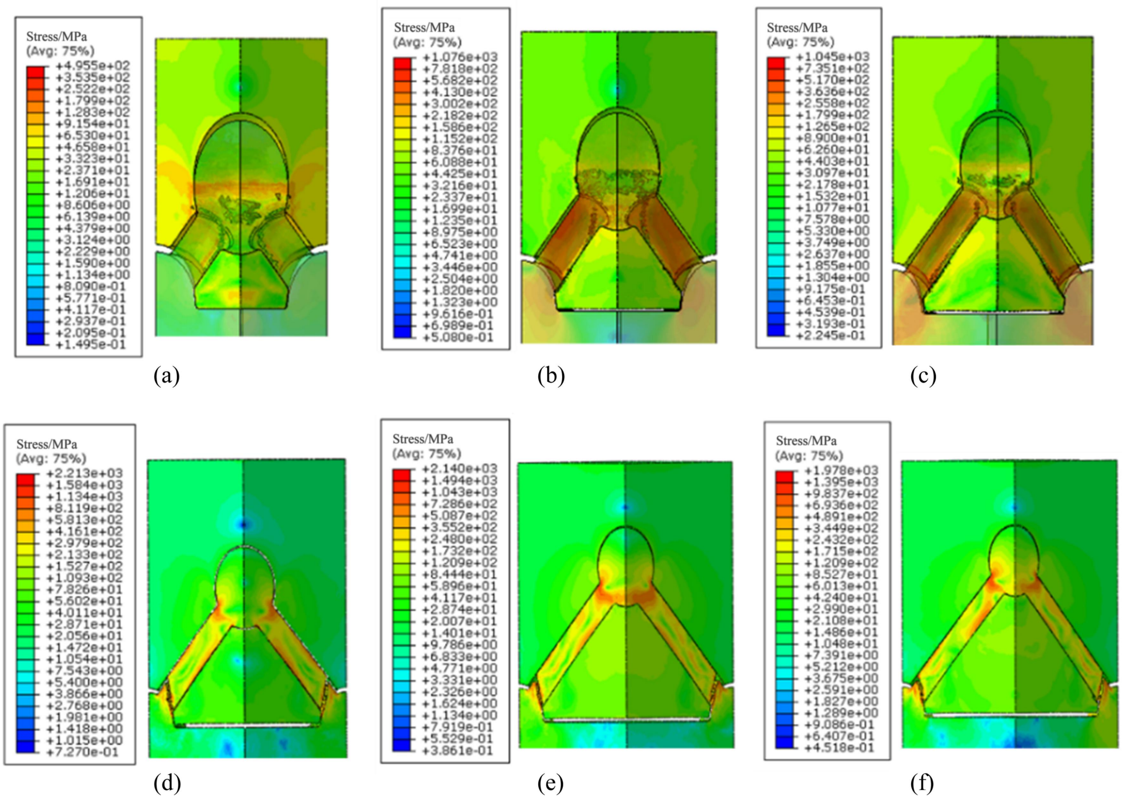

Fig. 9 Contour plot of von-Mises equivalent stress for Mg/Ti bimetal composites with different strut length to diameter: (a) l/d=1; (b) l/d=2; (c) l/d=3; (d) l/d=4; (e) l/d=5; (f) l/d=6

the failure modes of the Mg/Ti bimetal composite are mainly composed of interface debonding, magnesium matrix destruction, and fracture of titanium struts. In this study, interface debonding is not considered because it occurs before the destruction of magnesium or titanium in the loading process once the stress transmitted by the magnesium matrix is greater than weak interface bonding strength. The failure mode transformed from the destruction of the magnesium matrix to the breakage of titanium struts when the l/d is over 3, and the failure strength of the composite decreases. It is because the cross-section stress near the lower node exceeds the strength limit of titanium (σ_b) when the l/d is larger than 3, which leads to the fracture of struts.

4.3 Strengthening mechanism of lattice structure

Taking the tensile stress−strain curve of the lattice structure with the strut length-to-diameter ratio (l/d) is 3 as an example, as shown in Fig. 10, the damage process of the Mg/Ti bimetal composite will be analyzed. Figure 11 displays the contour plot of the stress corresponding to each stage. The entire deformation process can be divided into four stages. In stage I, both magnesium and titanium

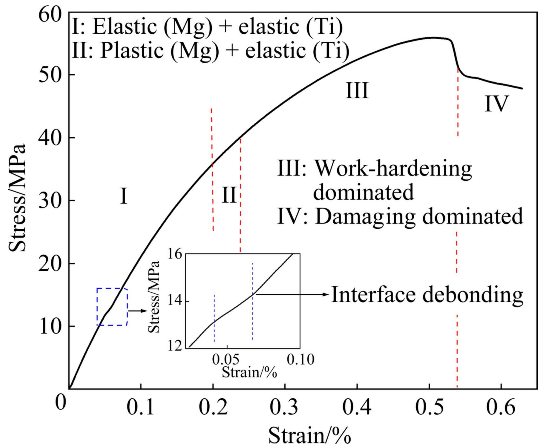

Fig. 10 Variations in tensile stress−strain curve for four stages of deformation process in composite Ti/Mg bimetal joint

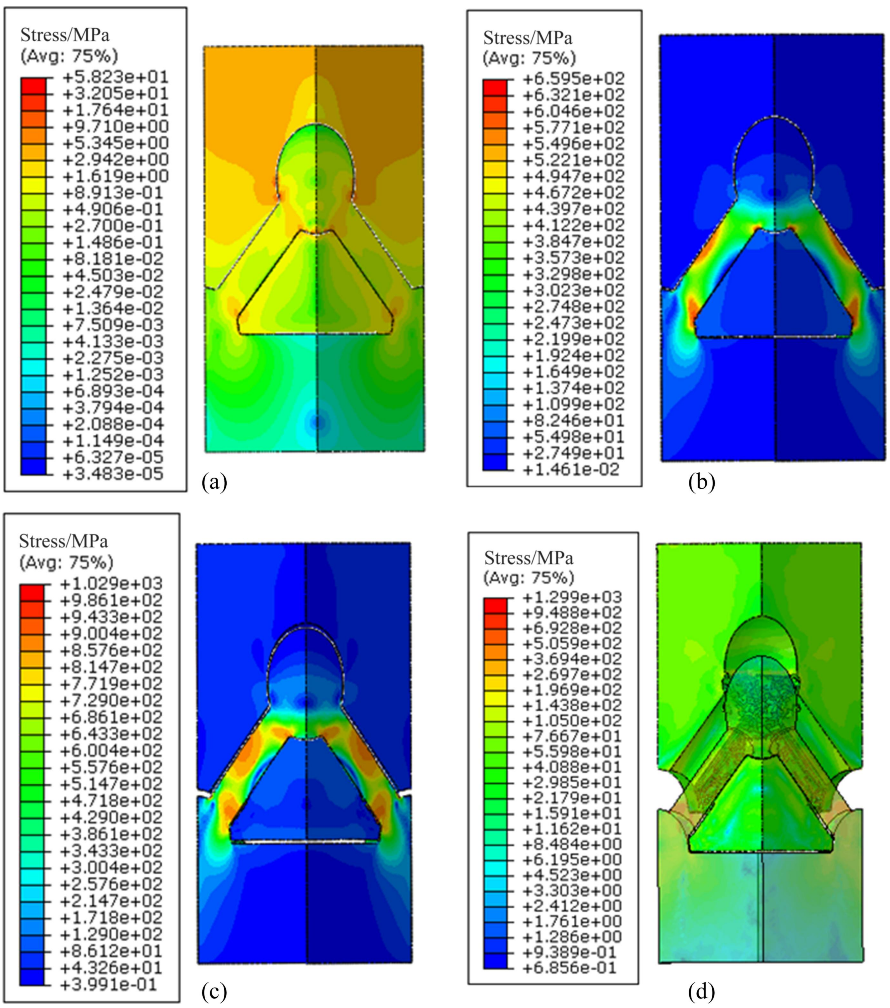

Fig. 11 Contour plot of stress during damage process: (a) Elastic deformation stage; (b) Mixed deformation stage and interface debonding; (c) Plastic deformation and work-hardening stage; (d) Damage continuation stage

lattices are principally deformed elastically as shown in Fig. 11(a). The initiation of global plastic deformation in the magnesium can be determined from the initial yielding of the composite, which occurs at ~42 MPa. It should be noted that the stress in the nodal regions, especially the transition of the node and strut is greater due to the effects of stress concentration. An obvious inflection point appears in the stress−strain curve during the elastic deformation stage, which is attributed to the interface debonding. After the plastic deformation of magnesium, the composite presents a mixed deformation mode of magnesium plasticity and titanium lattice elasticity (stage II in Fig. 11(b)). In stage III as shown in Fig. 11(c), both constituents are plastically deformed and work-hardened. During this stage, whether the failure mode is the fracture of the titanium lattice or damage of the magnesium matrix depends on whether the stress of the critical section of the strut exceeds the strength limit of titanium (1058 MPa). It shows that the titanium strut does not fracture when the ratio of strut length to diameter is less than or equal to 3. After reaching the maximum of stress, the true stress begins to decrease because of diminished work hardening and the evolution of irreversible damage (Stage IV in Fig. 11(d)).

Figure 12(a) presents the geometrical unit model and parameters of the Mg/Ti bimetal composite. When the model is subjected to tensile stress, σ_z, only the upper node is free to move in the z-direction. Figure 12(b) shows the simplified mechanical analysis model of a strut. Surface-1 and surface-2 represent half of the upper and lower surface of the titanium strut contacted with the magnesium, respectively. The composite undergoes elastic deformation before the interface debonding and the stress applied to the strut is mainly transmitted by the elastic deformation of the magnesium, and surface-1 and surface-2 suffer from tensile and compressive stress, respectively. When the interface stress exceeds the bonding strength (25 MPa), the interface stress is discontinuous and interface cracks start to appear. However, the stress of the strut suffered is mainly the compressive stress from surface-2.

The resultant stress applied to the strut is simplified to the center of the upper node, A. The strut is always deformed by a combination of stretching and bending. As a result of symmetry, each of the struts can be considered as a cantilever beam subjected to the same axial strengthening force F_N, bending moment M_1, and shear load F_1 [40]. Based on classical beam theory, the section near the lower node is the dangerous section, and its total stress can be written approximately as

$$\delta_{\max}=\frac{F_N}{A}+\frac{M_1}{W_z}=\frac{4F_z\sin\omega}{\pi d^2}+\frac{32lF_z\cos\omega}{\pi d^3} \tag{6}$$

where W_z is the bending section coefficient of a circle ($\pi d^3/32$). Under the same lattice structure and tensile stress (F_z, d, and ω are constant), the strut length is proportional to the section stress. In this study, the dangerous section stress of the strut is less than its strength limit when the strut length-to-diameter is less than or equal to 3, and the strut will not fracture. It is found that when the failure mode of the Mg/Ti bimetal composite is the fracture of the strut, the failure strength is smaller than that of the damage of the magnesium matrix.

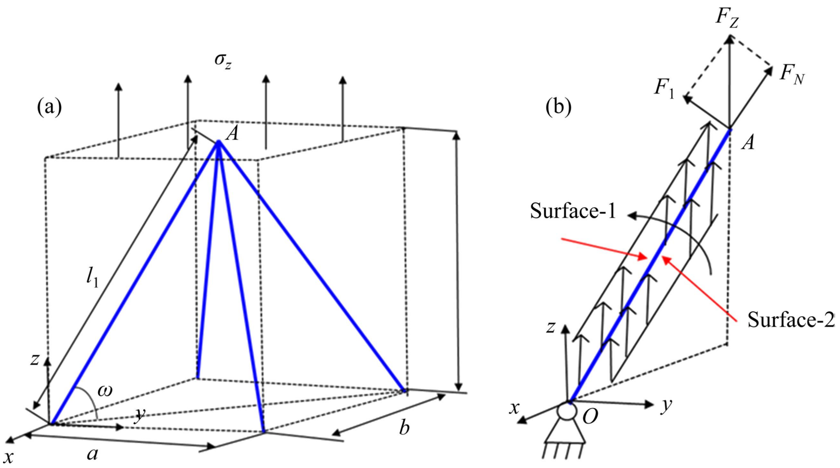

Fig. 12 Schematic diagram of force analysis of composites: (a) Geometrical parameters of Mg/Ti bimetal composite unit model; (b) Simplified mechanical analysis model of strut

4.4 Experimental verification

To verify the above simulation results, the representative lattice structures with l/d of 2, 3, and 5 were selected for experiments. Figure 13 shows the lattice structure specimen manufactured by SLM and cut by wire-electrode with the following dimensions: length is 57 mm, width is 30 mm, height is 35 mm, and the ratios of length to diameter (l/d) of lattice structure is 2, 3, and 5, respectively. The other geometrical parameters are constants with that obtained by orthogonal optimization (d=1, d_1/d=2.5, d_2/d=2.5).

Figure 14 shows the SEM images of the cross-section of as-cast Mg/Ti bimetal joints, in which the l/d of lattice structure is 2, 3, and 5, corresponding to Figs. 14(a−c), respectively. It can be seen that there are no obvious pores in the joints, which indicates that the AZ91D alloy melt penetrates the lattice structure well by the ultrasonic-assisted casting method.

Figure 15(a) shows the experimental tensile specimen obtained by sampling from the bimetallic composite ingots according to the specimen size shown in Fig. 7(b), in which the left of the specimen is TC4 and the right is AZ91D. Figure 15(b) shows the tensile load−displacement curves of the Mg/Ti bimetal composites with l/d of 2, 3, and 5. The maximum load value is 2425.47 N

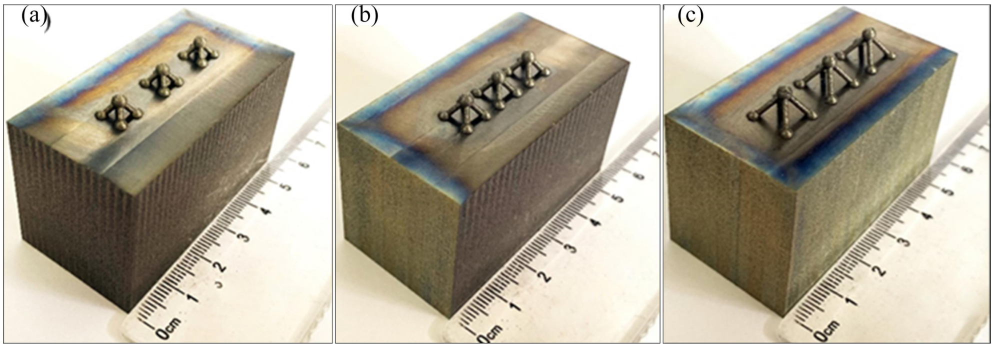

Fig. 13 Geometry of lattice structure manufactured by SLM: (a) l/d=2; (b) l/d=3; (c) l/d=5

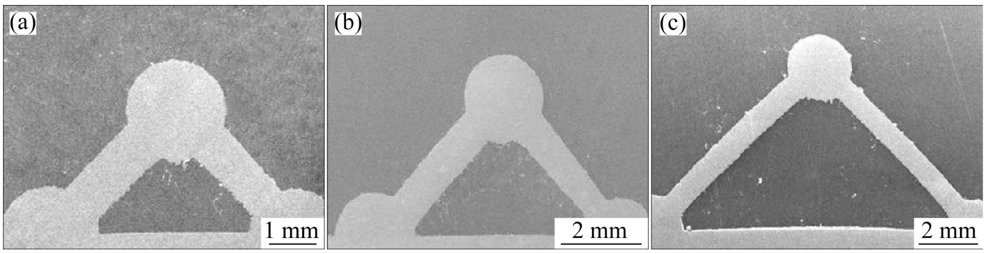

Fig. 14 Cross-sectional images of Mg/Ti bimetal joints: (a) l/d=2; (b) l/d=3; (c) l/d=5

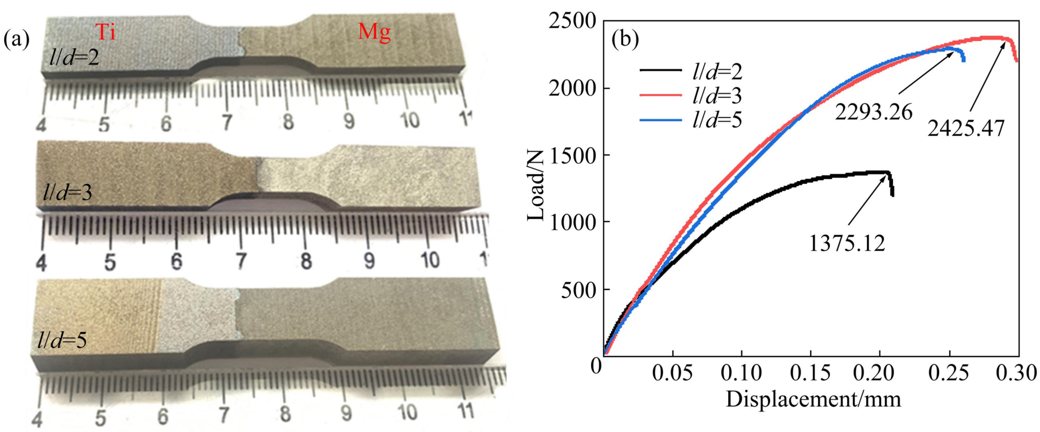

Fig. 15 Tensile specimens and load−displacement curves obtained by experiment: (a) Tensile specimen of each lattice structure (l/d=2, 3, 5); (b) Tensile load−displacement curves of Mg/Ti bimetal composites with l/d of 2, 3, and 5

when l/d is 3. The load−displacement curve shows the same variation trend as the simulated stress−strain curve (Fig. 10). Each curve has an inflection point corresponding to interface debonding.

To compare the experimental results with the simulation results, the experimental maximum load value was divided by the cross-section area of the composite within the distance of the tensile specimen, which was defined as the failure strength of the composite. Figure 16 shows the comparison results. The failure strength of the Mg/Ti bimetal composites increases first and then decreases with the increase of l/d, and it reaches a peak value when l/d is 3. The failure strength of the Mg/Ti bimetal joint with the optimal lattice structure is 77.34 MPa. The variation trend of failure strength with l/d obtained by experiments is consistent with that of FE analysis results. The mechanical properties of lattice structure and interface adhesion strength are of crucial importance for the behavior of the Mg/Ti bimetal composites. When the strut diameter (d) is constant, the strut length (l) is proportional to the section stress far from the loading position. Experimental and simulation results show that when l/d is over 3, the strut fractures under a low load value. The lattice structure with l/d=3 has a higher surface area than the lattice structure with l/d=2, which indicates that the failure strength increases with an increased surface area of the lattice structure.

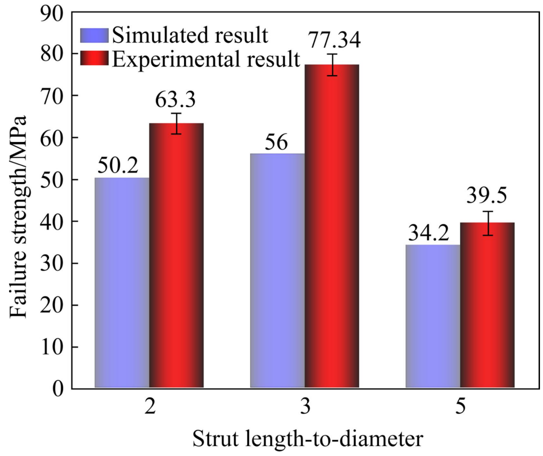

Fig. 16 Comparison of experimental and simulated results

Figure 17 shows the comparison of failure modes. The failure modes obtained by the experiment are in good agreement with the FE analysis results. The failure mode is the damage of magnesium when l/d is 2 and 3, while it transforms to the fracture of TC4-strut when l/d is over 3. As shown in Figs 17(a) and (b), the damage of magnesium is characterized by cracking and separating into two parts, respectively. During the deformation process of the Mg/Ti bimetal composites, the stress transfer is discontinuous after the interface debonding, and magnesium and TC4-strut squeeze each other. At this time, the incompatibility of deformation between the two

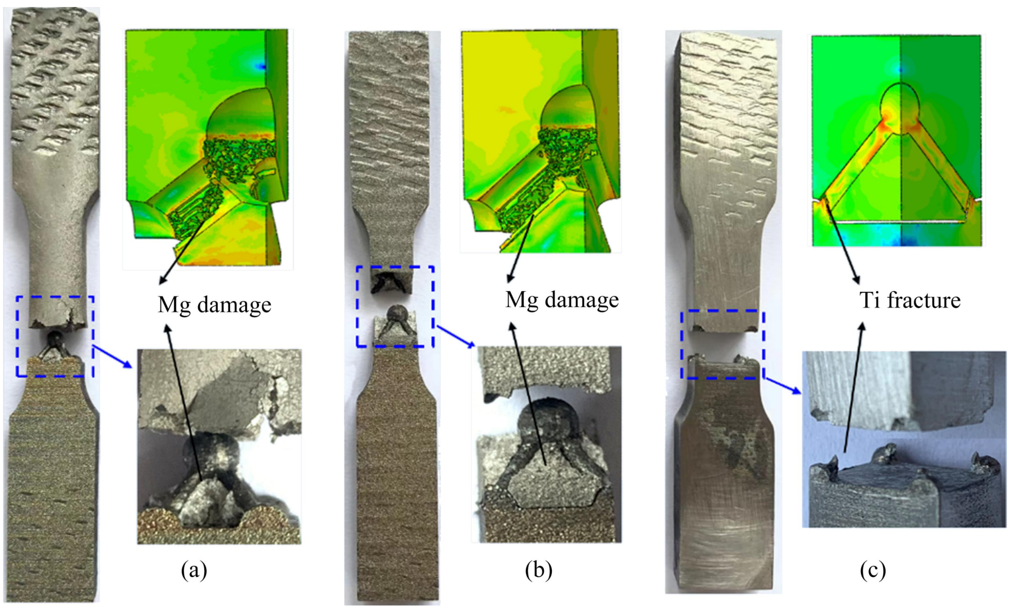

Fig. 17 Comparison of failure modes of Mg/Ti bimetal composites obtained by experiment and FE simulation: (a) l/d=2; (b) l/d=3; (c) l/d=5

materials results in increased local stress and eventually cracks at the grain boundary of the Mg matrix. In Fig. 17(c), the fracture section of the TC4-strut is far away from the loading position because the shear fracture is caused by the combination of tensile and bending deformation.

Moreover, it can be found from the failed samples that the lattice structure is filled with magnesium, so the mechanical interlocking of magnesium and titanium can be realized by the ultrasonic vibration-assisted SLCC. The interface detached completely indicating that there is no reaction or atomic diffusion between Mg and Ti during the whole process [15].

5 Conclusions

(1) The optimized geometric parameters of the lattice structure are the strut diameter (*d*) of 1 mm, the ratio of strut length to diameter (*l*/*d*) of 3, and the ratios of the upper and lower node to diameter (d_1/d and d_2/d) of 2.5 and 2.5, respectively. The failure strength of the Mg/Ti bimetal joint with the optimal lattice structure is 77.3 MPa.

(2) The ratio of strut length to diameter (*l*/*d*) is the significant factor affecting failure strength. Experimental and FE analysis results have shown that failure strength increases first and then decreases with the increase of *l*/*d*. The failure strength reaches a peak value when *l*/*d* is 3.

(3) The failure mode of the Mg/Ti bimetal composites consists of interface debonding, damage of magnesium, and fracture of the titanium strut. Interface debonding occurs before matrix failure, and the failure mode changes from the damage of the magnesium matrix to the fracture of the titanium strut with the increase of *l*/*d*.

CRediT authorship contribution statement

Yuan-bing WU: Methodology, Formal analysis, Investigation, Writing – Original draft; **Jian-hua ZHAO:** Resources, Funding acquisition, Supervision; **Wei-li PENG:** Methodology, Data curation, Software; **Cheng GU:** Formal analysis, Writing – Review & editing; **Jin CHENG:** Conceptualization, Writing – Review; **Ya-jun WANG:** Formal analysis, Methodology.

Declaration of competing interest

The authors declare that they have no known competing financial interests or personal relationships that could have appeared to influence the work reported in this paper.

Acknowledgments

This work was supported by Graduate Scientific Research and Innovation Foundation of Chongqing, China (No. CYB21005), the National Natural Science Foundation of China (No. 51875062), and China Postdoctoral Science Foundation (No. 2021M700567).

References

[1] WU Zhao-xuan, CURTIN W A. The origins of high hardening and low ductility in magnesium [J]. Nature, 2015, 526: 62−67.

[2] PHETSINORATH S, ZOU Jian-xin, ZENG Xiao-qin, SUN Hai-quan, DING Wen-jiang. Preparation and hydrogen storage properties of ultrafine pure Mg and Mg−Ti particles [J]. Transactions of Nonferrous Metals Society of China, 2012, 22: 1849−1854.

[3] CAI Xue-cheng, DING Shuai-jun, LI Zhong-jie, ZHANG Xin, WEN Kang-kang, XU Li-dong, ZHANG Yang, SHEN Tong-de. Mg−Ti composites fabricated by a novel one-step high-pressure sintering: The correlation between microstructures and mechanical properties [J]. Composites: Part B, Engineering, 2021, 215: 108743.

[4] ZHAO Jian-hua, SHANGGUAN Jing-jing, GU Cheng, JIN Bing-yan, SHI Yu. Microstructures and mechanical properties of TC4/AZ91D bimetal prepared by solid–liquid compound casting combined with Zn/Al composite interlayer [J]. Transactions of Nonferrous Metals Society of China, 2022, 32: 1144−1158.

[5] CAI Xue-cheng, DING Shuai-jun, LI Zhong-jie, ZHANG Xin, WEN Kang-kang, XU Li-dong, ZHANG Yang, PENG Yan, SHEN Tong-de. Simultaneous sintering of low-melting-point Mg with high-melting-point Ti via a novel one-step high-pressure solid-phase sintering strategy [J]. Journal of Alloys and Compounds, 2021, 858: 158344.

[6] OUYANG Si-hui, HUANG Qian-li, LIU Yong, OUYANG Zheng-xiao, LIANG Lu-xin. Powder metallurgical Ti−Mg metal-metal composites facilitate osteoconduction and osseointegration for orthopedic application [J]. Bioactive Materials, 2019, 4: 37−42.

[7] TAN Cai-wang, YANG Jia, ZHAO Xiao-ye, ZHANG Kai-ping, SONG Xiao-guo, CHEN Bo, LI Li-qun, FENG Ji-cai. Influence of Ni coating on interfacial reactions and mechanical properties in laser welding-brazing of Mg/Ti butt joint [J]. Journal of Alloys and Compounds, 2018, 764: 186−201.

[8] ATIEH A M, KHAN T I. TLP bonding of Ti−6Al−4V and Mg−AZ31 alloys using pure Ni electro-deposited coats [J]. Journal of Materials Processing Technology, 2014, 214: 3158−3168.

[9] LI Rui-di, LI Jing-long, XIONG Jiang-tao, ZHANG Fu-sheng, ZHAO Ke, JI Cheng-zhong. Friction heat production and atom diffusion behaviors during Mg−Ti

rotating friction welding process [J]. Transactions of Nonferrous Metals Society of China, 2012, 22: 2665−2671.

[10] WANG Peng-ju, HUANG Hong-tao, LIU Jiang-jiang, LIU Qing, CHEN Ze-jun. Microstructure and mechanical properties of Ti6Al4V/AA6061/AZ31 laminated metal composites (LMCs) fabricated by hot roll bonding [J]. Journal of Alloys and Compounds, 2021, 861: 157943.

[11] ZHAO Jian-hua, ZHAO Wen-qun, QU Shen, ZHANG Yan-qing. Microstructures and mechanical properties of AZ91D/0Cr19Ni9 bimetal composite prepared by liquid-solid compound casting [J]. Transactions of Nonferrous Metals Society of China, 2019, 29: 51−58.

[12] LI Guang-yu, YANG Wen-chao, JIANG Wen-ming, GUAN Feng, JIANG Hai-xiao, WU Yao, FAN Zi-tian. The role of vacuum degree in the bonding of Al/Mg bimetal prepared by a compound casting process [J]. Journal of Materials Processing Technology, 2019, 265: 112−121.

[13] LI Guang-yu, JIANG Wen-ming, GUAN Feng, ZHU Jun-wen, YU Yang, FAN Zi-tian. Improving mechanical properties of AZ91D magnesium/A356 aluminum bimetal prepared by compound casting via a high velocity oxygen fuel sprayed Ni coating. Journal of Magnesium and Alloys, 2022, 10: 1075−1085.

[14] LI Guang-yu, JIANG Wen-ming, GUAN Feng, ZHU Jun-wen, ZHANG Zheng, FAN Zi-tian. Microstructure, mechanical properties and corrosion resistance of A356 aluminum/AZ91D magnesium bimetal prepared by a compound casting combined with a novel Ni-Cu composite interlayer [J]. Journal of Materials Processing Technology, 2021, 288: 116874.

[15] WEN Fu-lin, ZHAO Jian-hua, YUAN Miao-wang, WANG Jing-feng, ZHENG Deng-zhi, ZHANG Jin-yong, HE Ke, SHANGGUAN Jing-jing, GUO Yu. Influence of Ni interlayer on interfacial microstructure and mechanical properties of Ti−6Al−4V/AZ91D bimetals fabricated by a solid–liquid compound casting process [J]. Journal of Magnesium and Alloys, 2021, 9: 1382−1395.

[16] ZHANG Ze-qun, TAN Cai-wang, WANG Gang, CHEN Bo, SONG Xiao-guo, ZHAO Hong-yun, LI Li-qun, FENG Ji-cai. Laser welding-brazing of immiscible AZ31B Mg and Ti−6Al−4V alloys using an electrodeposited Cu interlayer [J]. Journal of Materials Engineering and Performance, 2018, 27: 1414−1426.

[17] WEN Fu-lin, ZHAO Jian-hua, FENG Kai-qing, YUAN Miao-wang, ZHENG Deng-zhi, GU Cheng, XU Bei. Investigation of Cu interlayer on joint formation of Ti/Mg bimetal fabricated by liquid–solid compound casting process [J]. Metals and Materials International, 2022, 28: 1711−1724.

[18] ATIEH A M, KHAN T I. Application of Ni and Cu nanoparticles in transient liquid phase (TLP) bonding of Ti−6Al−4V and Mg-AZ31 alloys [J]. Journal of Materials Science, 2014, 49: 7648−7658.

[19] SHANGGUAN Jing-jing, ZHAO Jian-hua, SHI Yu, GU Cheng, JIN Bing-yan, CHENG Jin, GUO Yu. Effects of Zn interlayer on microstructures and mechanical properties of TC4/AZ91D bimetal via solid–liquid compound casting process [J]. International Journal of Metalcasting, 2022, 16: 419−434.

[20] NIE Hui-hui, ZHENG Liu-wei, KANG Xiao-ping, HAO Xin-wei, LI Xian-rong, LIANG Wei. In-situ investigation of deformation behavior and fracture forms of Ti/Al/Mg/Al/Ti laminates [J]. Transactions of Nonferrous Metals Society of China, 2021, 31: 1656−1664.

[21] ZHAO Jian-hua, SHANGGUAN Jing-jing, GAO Li-sen, GU Cheng, WANG Ya-jun, SHI Yu. New insights into microstructure characteristics and tribological property of Ti alloy processed by hot-dip aluminizing and heat treatment [J]. Metallurgical and Materials Transactions A: Physical Metallurgy and Materials Science, 2022, 53: 1035−1050.

[22] XU Shan-qing, SHEN Jian-hu, ZHOU Shi-wei, HUANG Xiao-dong, XIE Yi-min. Design of lattice structures with controlled anisotropy [J]. Materials & Design, 2016, 93: 443−447.

[23] MARCO M, BELDA R, MIGUÉLEZ M H, GINER E. Numerical analysis of mechanical behaviour of lattice and porous structures [J]. Composite Structures, 2021, 261: 113292.

[24] OZDEMIR Z, HERNANDEZ-NAVA E, TYAS A, WARREN J A, FAY S D, GOODALL R, TODD I, ASKES H. Energy absorption in lattice structures in dynamics: Experiments [J]. International Journal of Impact Engineering, 2016, 89: 49−61.

[25] WANG Xiao-jian, XU Shan-qing, ZHOU Shi-wei, XU Wei, LEARY M, CHOONG P, QIAN M, BRANDT M, XIE Yi-min. Topological design and additive manufacturing of porous metals for bone scaffolds and orthopaedic implants: A review [J]. Biomaterials, 2016, 83: 127−141.

[26] MOHAMMADI M, SADEGHI A. Progressive damage and failure modeling in composite cylindrical pyramidal lattice structure [J]. Proceedings of the Institution of Mechanical Engineers, Part L: Journal of Materials: Design and Applications, 2020, 234: 1515−1525.

[27] LI Xiu-hui, GHASRI-KHOUZANI M, BOGNO A A, LIU Jing, HENEIN H, CHEN Zeng-tao, QURESHI A J. Investigation of compressive and tensile behavior of stainless steel/dissolvable aluminum bimetallic composites by finite element modeling and digital image correlation [J]. Materials, 2021, 14: 3654.

[28] SUN Xiao-jing, JIANG Feng-chun, YUAN Ding, WANG Gui-dong, TONG Yun-xiang, WANG Jian-dong. High damping capacity of AlSi10Mg−NiTi lattice structure interpenetrating phase composites prepared by additive manufacturing and pressureless infiltration [J]. Journal of Alloys and Compounds, 2022, 905: 164075.

[29] RAIMONDI L, TOMESANI L, DONATI L, ZUCCHELLI A. Lattice material infiltration for hybrid metal-composite joints: Manufacturing and static strength [J]. Composite Structures, 2021, 269: 114069.

[30] CHENG Jia-hao, GUSSEV M, ALLEN J, HU Xiao-hua, MOUSTAFA A R, SPLITTER D A, SHYAM A. Deformation and failure of PrintCast A356/316L composites: Digital image correlation and finite element modeling [J]. Materials & Design, 2020, 195: 109061.

[31] MAZUR M, LEARY M, SUN Shou-jin, VCELKA M, SHIDID D, BRANDT M. Deformation and failure behaviour of Ti−6Al−4V lattice structures manufactured by selective laser melting (SLM) [J]. The International Journal of

Advanced Manufacturing Technology, 2016, 84: 1391−1411.

[32] Abaqus/CAE 6.14 User''s Manual [EB/OL]. https://www.scopus.com/inward/record.uri?eid=2-s2.0-85089823156&partnerID=40&md5=a05a511616dc358e75723ebf30084b49.

[33] SAREMIAN R, BADROSSAMAY M, FOROOZMEHR E, KADKHODAEI M, FOROOGHI F. Experimental and numerical investigation on lattice structures fabricated by selective laser melting process under quasi-static and dynamic loadings [J]. The International Journal of Advanced Manufacturing Technology, 2021, 112: 2815−2836.

[34] LIU S Y, SHIN Y C. Additive manufacturing of Ti6Al4V alloy: A review [J]. Materials & Design, 2019, 164: 107552.

[35] OMURA N, MURAKAMI Y, LI Ming-jun, TAMURA T, MIWA K J, FURUKAWA H, HARADA M, YOKOI M. Effects of mechanical vibration on macrostructure and mechanical properties of AC4C aluminum alloy castings [J]. Materials Transactions, 2009, 50: 2578−2583.

[36] BUTLER C. A primer on the Taguchi method [J]. Computer Integrated Manufacturing Systems, 1992, 5: 246.

[37] ZIEGEL E R, ROSS P. Taguchi techniques for quality engineering [J]. Technometrics, 1997, 39: 109−110.

[38] HARTZELL F Z. Statistical methods for research workers [J]. Agronomy Journal, 1945, 37: 242.

[39] YOUSEFIEH M, SHAMANIAN M, SAATCHI A. Optimization of the pulsed current gas tungsten arc welding (PCGTAW) parameters for corrosion resistance of super duplex stainless steel (UNS S32760) welds using the Taguchi method [J]. Journal of Alloys and Compounds, 2011, 509: 782−788.

[40] USHIJIMA K, CANTWELL W J, MINES R A W, TSOPANOS S, SMITH M. An investigation into the compressive properties of stainless steel micro-lattice structures [J]. Journal of Sandwich Structures & Materials, 2011, 13: 303−329.

增材制造钛基金字塔点阵结构对镁/钛双金属复合材料界面强化的优化

吴远兵 [1]，赵建华 [1,2]，彭韦力 [1]，辜 诚 [1,2]，程 进 [1]，王亚军 [1,2]

1. 重庆大学 材料科学与工程学院，重庆 400045；
2. 重庆大学 国家镁合金工程研究中心，重庆 400044

摘 要：采用超声辅助固−液复合铸造的方法，通过在界面处采用增材制造的钛基金字塔型点阵材料制备镁/钛异种双金属复合材料。采用正交法对点阵结构参数进行优化。结果表明，优化后的点阵结构参数为：杆直径(d) 1 mm，杆长与杆直径比(l/d) 3，上节点和下节点直径与杆直径比(d_1/d, d_2/d)均为 2.5，其中 l/d 是影响接头失效强度的最显著因素，最优点阵结构参数下镁/钛双金属接头的失效强度为 77.3 MPa。实验结果和有限元分析表明：随着点阵结构长径比的增加，镁/钛双金属接头的失效强度先增加后减小，当长径比为 3 时，失效强度达到最大。

关键词：镁/钛双金属复合材料；金字塔点阵结构；优化；增材制造；失效强度；有限元分析

(Edited by Xiang-qun LI)